



# Heterogeneous molecular rhenium catalyst for CO<sub>2</sub> photoreduction with high activity and tailored selectivity in an aqueous solution



Shengbo Zhang<sup>a,b</sup>, Mei Li<sup>b</sup>, Wenjun Qiu<sup>b</sup>, Jinyu Han<sup>b</sup>, Hua Wang<sup>b</sup>, Xiao Liu<sup>a,\*</sup>

<sup>a</sup> Key Laboratory of Pesticide & Chemical Biology of Ministry of Education, College of Chemistry, Central China Normal University, Wuhan 430079, China

<sup>b</sup> Key Laboratory for Green Chemical Technology, School of Chemical Engineering and Technology, Tianjin University, Collaborative Innovation Center of Chemical Science and Engineering, Tianjin 300072, China

## ARTICLE INFO

**Keywords:**  
CO<sub>2</sub> photoreduction  
Heterogeneous molecular catalyst  
Organosilica nanotubes  
Microenvironment regulation  
Aqueous solution

## ABSTRACT

The effective molecular-catalyst-based device that converts CO<sub>2</sub> to value-added products is of significance but challenging. Herein, utilizing organosilica nanotubes as the solid chelating ligands, we successfully construct heterogeneous molecular rhenium catalysts for efficient CO<sub>2</sub> photoreduction to CO. The nanotube framework compositions and the microenvironment of the rhenium catalysts are finely regulated, aiming to enhance the catalytic selectivity and activity in water-containing systems. By adjusting bipyridine amounts and capping the surface silanols, the preferential adsorption for CO<sub>2</sub> over H<sub>2</sub>O around the active sites is realized. Relative to that of the unmodified catalyst, the CO selectivity increased greatly from 53% to 94% in water/acetonitrile. Furthermore, the heterogeneous molecular catalysts exhibit a total turnover number that is nine times higher than the corresponding homogeneous one (134 versus 15). Using *in situ* infrared spectroscopy and density functional theory calculations, a reasonable mechanism for high CO selectivity in the presence of H<sub>2</sub>O is demonstrated.

## 1. Introduction

The photocatalytic reduction of CO<sub>2</sub>, which mimics natural photosynthesis, aims to achieve efficient light-to-chemical transformation [1–5]. The most serious challenge in this process is the activation of CO<sub>2</sub> molecules because of its large potential of the CO<sub>2</sub>/CO<sub>2</sub><sup>−</sup> redox couple (−1.9 V *versus* the normal hydrogen electrode (NHE)). An effective alternative to activate CO<sub>2</sub> is the proton-assisted multielectron catalytic processes, such as CO<sub>2</sub> + 2H<sup>+</sup> + 2e<sup>−</sup> = CO + H<sub>2</sub>O (E' = −0.53 V), which requires much less energy [6–11]. Considering the multiple accessible redox states, transition-metal complexes could be utilized as catalysts to minimize the overpotentials for the efficient reduction of CO<sub>2</sub>. Given this, the device designs for artificial photosynthesis (AP) based on molecular catalysts have always been attracted much research attention [12–15]. However, the molecule-assembled AP systems usually perform low stability and activity. Furthermore, photocatalytic CO<sub>2</sub> reduction using molecular catalysts is usually confined to non-aqueous solvent (CH<sub>3</sub>CN or DMF) systems, which is mainly because that reducing a proton to H<sub>2</sub> is more thermodynamically favorable than reducing CO<sub>2</sub> in water [16–19]. Given that a water-containing system is necessary to construct AP devices that couples CO<sub>2</sub> reduction and water oxidation, designing and developing molecular catalysts with

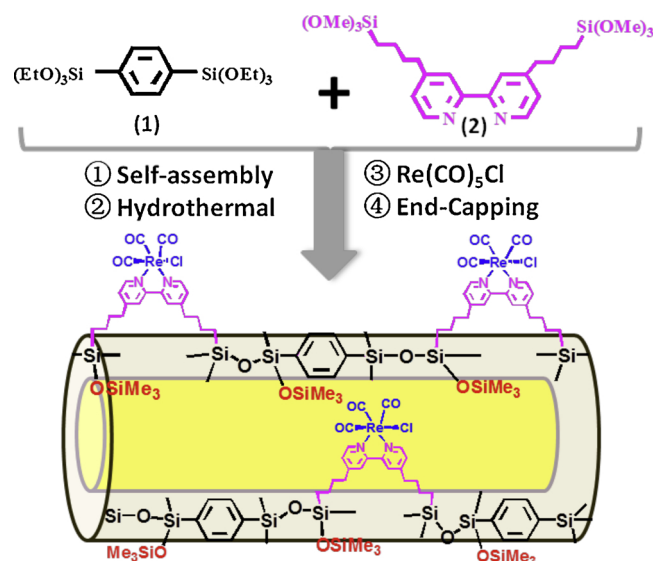
high selectivity and stability for the photocatalytic CO<sub>2</sub> reduction in a water-containing system are of high significance.

The incorporation of metal complex catalysts onto a solid matrix, such as metal organic frameworks (MOFs), covalent organic frameworks (COFs) and periodic mesoporous organosilicas (PMOs) might be a promising way to design AP devices for efficient CO<sub>2</sub> photoreduction [20–28]. On the one hand, heterogenization can make active sites spatial isolation and prevent the molecular catalyst deactivation. On the other hand, the matrix framework compositions could be adjusted to preferentially adsorb CO<sub>2</sub> rather than water molecules, thus tailoring the catalytic activity and selectivity in water-containing systems.

Recently, chelating-ligand-incorporated organosilica nanotubes were prepared from bridged organosilane precursors for the efficient heterogeneous molecular catalyst design in our group [29–34]. These nanotubes with mesoporous diameters have distinct advantages, including various organic functionalities in the nanotube frameworks, high surface areas, fast diffusion of substrates in the tubes, and tunable hydrophilicity/hydrophobicity. Herein, using benzene-bridged organosilica nanotubes containing bipyridine ligands (BPY-NT) as the platform, we report the direct construction of a rhenium complex on the nanotube walls (Re-BPY-NT) through metal complexation for photocatalytic reduction of CO<sub>2</sub>. By carefully adjusting the bipyridine

\* Corresponding author.

E-mail address: liuxiao71@tju.edu.cn (X. Liu).



**Scheme 1.** Synthetic routes for the design of heterogeneous molecular Re-based catalysts on organosilica nanotubes (Re-BPy<sub>0.3</sub>-NT-Me).

contents in the framework, the heterogeneous molecular-catalyst-based nanotubes (Re-BPy<sub>0.3</sub>-NT) could not only facilitate the rapid diffusion of reactants and products but also increase the adsorption capacity of CO<sub>2</sub>. In order to further inhibit protons from reaching the active sites to produce H<sub>2</sub>, the remaining accessible surface silanols groups (Si-OH) of the organosilica nanotubes were capped using trimethylsilyl [-Si(CH<sub>3</sub>)<sub>3</sub>] (Re-BPy<sub>0.3</sub>-NT-Me) to increase the hydrophobicity (**Scheme 1**). The as-prepared Re-BPy<sub>0.3</sub>-NT-Me shows higher catalytic activity, CO selectivity, and a turnover number (TON) compared with those of the unmodified catalyst and even the corresponding homogeneous one in the CO<sub>2</sub> photoreduction system with a high concentration of water.

## 2. Experimental section

### 2.1. Synthesis of Re-BPy<sub>0.3</sub>-NT-Me

The rhenium-immobilized nanotube catalysts were prepared by adding BPy-NT (300 mg) to a solution of Re(CO)<sub>5</sub>Cl (40 mg) in 60 mL of toluene under nitrogen atmosphere. After the suspension was stirred under refluxing conditions for 24 h, the solid phase was obtained by filtration and washed with acetone. The dried samples were named as Re-BPy<sub>0.3</sub>-NT. Then, 2.0 g of Re-BPy<sub>0.3</sub>-NT and 8 mL of [(CH<sub>3</sub>)<sub>3</sub>Si]<sub>2</sub>NH in 30 mL of dry toluene were stirred at room temperature overnight. The resultant powder was filtered, washed and dried under vacuum overnight at 60 °C. The dried samples were named as Re-BPy<sub>0.3</sub>-NT-Me.

### 2.2. Re-BPy<sub>0.3</sub>-NT-Me-photocatalyzed CO<sub>2</sub> reduction reaction

In a typical experiment, Re-BPy-NT-Me (2.9 μmol Re) was added to a fresh 40 mL mixed solution containing 17.5 mL of acetonitrile, 20 mL of water and 2.5 mL of triethanolamine. This system was purged with CO<sub>2</sub> for 1.0 h. The reaction was operated at the room temperature with a visible light ( $\lambda > 420$  nm) illumination. The gas molecules generated in the head space were periodically analyzed quantitatively by a Bruker 456 gas chromatograph equipped with a thermal conductivity detector (TCD).

### 2.3. Characterizations

Transmission electron microscopy (TEM) were operated on a JEM-2100 F system operating at 200 kV. The morphology of these catalysts were analysed by scanning electron microscopy (SEM) using Hitachi S-

4800 scanning electron microscope (SEM, 5 kV) equipped with the Thermo Scientific energy-dispersion X-ray fluorescence analyser. N<sub>2</sub> adsorption-desorption isotherms were tested at -196 °C on a Micromeritics Tristar 3000 instrument. The specific surface area was obtained by the Brunauer–Emmett–Teller method; the pore size distribution was obtained by the Barrett–Joyner–Halenda method using the adsorption branch. Carbon, hydrogen and nitrogen contents were determined via CHN elemental analysis (vario EL CUBE). UV/vis absorption and diffuse reflectance spectra were obtained using Instant Spec BWS003 spectrometers. Re L<sub>III</sub>-edge extended X-ray absorption fine structure (EXAFS) spectra were collected at the beamline 1W1B of Beijing Synchrotron Radiation Facility, Institute of High Energy Physics, Chinese Academy of Sciences. The beamline was equipped with a Si (111) double crystal monochromator. The  $k^3$ -weighted EXAFS oscillations were Fourier transformed into R-space. Transient absorption spectroscopy (TAS) was carried out employing a Femtosecond-scale laser flash photolysis spectrometer (Applied Photophysics) equipped with the proper diffuse reflectance accessory. The samples were placed in a closed quartz cuvette, purged with N<sub>2</sub> and were excited with a 380 nm laser beam. FT-IR spectra were collected with a Bruker Vertex 80v. *In situ* IR spectra of a acetonitrile-water-triethanolamine (0.875:1:0.125, v/v) solution containing Re catalyst during photo-irradiation ( $\lambda > 420$  nm) under a CO<sub>2</sub> atmosphere. Solid-state <sup>13</sup>C cross polarization magic-angle spinning (CP MAS) NMR and <sup>29</sup>Si magic angle spinning (MAS) NMR spectra were collected on 400 MHz instruments. Photoluminescence spectra (PL) were done on Jobin Yvon Fluorolog3-21 spectrophotometer at an excitation wavelength of 380 nm by using the powder sample. Photoelectric properties measurements were carried out with an Autolab 302 N electrochemical system with a 300 W xenon lamp and used an Ag/AgCl (0.5 M Na<sub>2</sub>SO<sub>4</sub>) as the reference electrode and a Pt plate as the counter electrode. The photocurrent density vs time (I-t) curves of the prepared photoelectrodes were operated under an alternate light irradiation (light on/off cycles: 30 s). Mott–Schottky measurements of the catalysts were conducted in an Autolab 302 N electrochemical system at frequencies of 500, 1000, and 1500 Hz. In Mott–Schottky measures, a three-electrode configuration was used with Pt plate as counter electrode, Ag/AgCl electrode as reference electrode and catalysts on FTO glass substrate as working electrode in 0.5 M Na<sub>2</sub>SO<sub>4</sub> electrolyte. Water contact angles were measured on the contact angle system OCA 20 by pressing the powder sample into a thin sheet.

### 2.4. DFT theoretical calculation

All the calculations were used spin-polarized density functional theory (DFT) with generalized gradient approximation (GGA) for exchange-correlation potential embedded in the Vienna Ab Initio Simulation Package (VASP). The ion-electron interaction was described with projector augmented wave (PAW) method. The cutoff energy of the plane-wave basis set was set at 500 eV. The cluster with periodic boundary condition was modeled with a large super cell of  $28 \times 28 \times 28$  Å<sup>3</sup>, eliminating the artificial interaction between molecular electrocatalysts in adjacent cells. The van der Waals (vdW) dispersion by employing the D3 method of Grimme was considered for all the calculation. The Brillouin zone integrations were performed by using Gamma  $1 \times 1 \times 1$  for geometric optimization. The convergence thresholds for structural optimization was set at 0.02 eV/Å in force. The convergence criterion for energy was  $10^{-5}$  eV.

## 3. Results and discussion

A rhenium complex was prepared, as shown in **Scheme 1**. First, organosilica nanotubes containing bipyridine ligands in the framework (BPy<sub>x</sub>-NT, where x corresponds to the molar ratio of precursors 2 in the initial total precursors) was synthesized as our previous report [29,33]. Subsequently, the rhenium complex [Re(CO)<sub>5</sub>Cl] was anchored on the

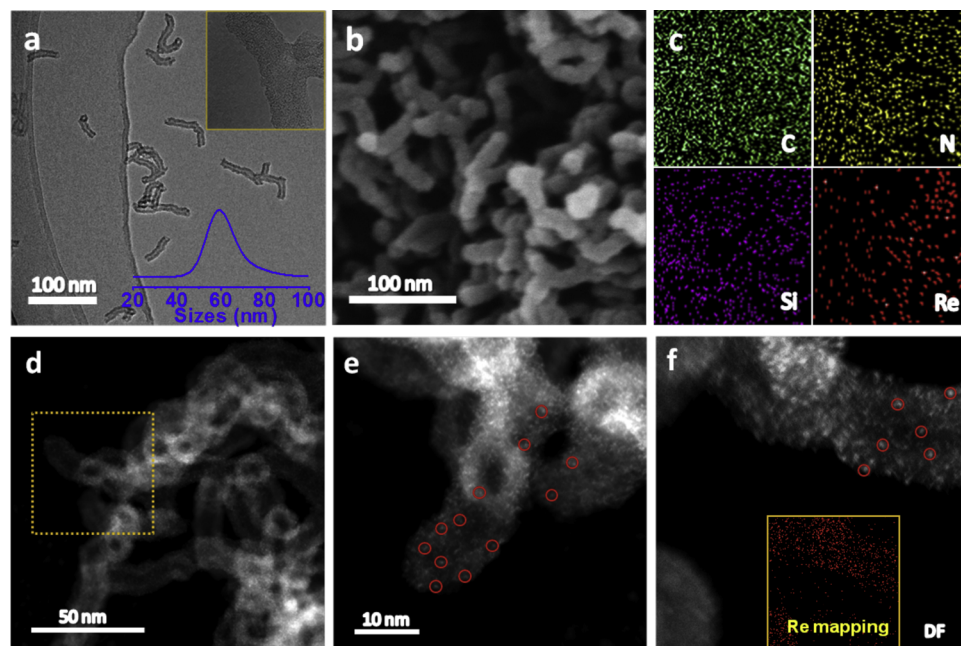


**Fig. 1.** (a) TEM, (b) SEM and (c) EDS mapping images of Re-BPy<sub>0.3</sub>-NT-Me. The inset graph in (a) shows the nanotube length distribution in ethanol obtained via dynamics light scattering and magnified high-resolution TEM. (d) Aberration-corrected HAADF-STEM and (e-f) magnified aberration-corrected HAADF-STEM and corresponding Re mapping images of Re-BPy<sub>0.3</sub>-NT-Me.

nanotube walls (denoted by Re-BPy<sub>0.3</sub>-NT) via the metal complexation of Re to the bipyridine unit in BPy<sub>0.3</sub>-NT (Figs. S1–5). Finally, the remaining accessible silanols (Si-OH) on the organosilica nanotubes were capped using trimethylsilyl [-Si(CH<sub>3</sub>)<sub>3</sub>] groups. The obtained sample was denoted by Re-BPy<sub>0.3</sub>-NT-Me. For comparison, the Re complex was also incorporated onto bipyridine-bridging organosilica nanotubes with fewer bipyridine groups, *i.e.*, BPy<sub>0.1</sub>-NT (denoted by Re-BPy<sub>0.1</sub>-NT) (Figs. S7–11) and pure silica nanotubes without phenyl groups (denoted by Re-BPy<sub>0.1</sub>-SNT) (Figs. S13–17).

Fig. 1a and b show the transmission electron microscopy (TEM) and scanning electron microscopy (SEM) images of the short nanotubes Re-BPy<sub>0.3</sub>-NT-Me. The TEM image clearly reveals that these catalysts comprise nanotubes with ~60 nm lengths and ~5–7 nm inner diameters. The SEM image further confirms the nanorod morphology. The energy-dispersive X-ray spectrometry (EDS) mapping analysis reveals that Re is uniformly distributed on the support (Fig. 1c). In order to more intuitively know the distribution of Re atoms, we performed aberration-corrected, high-angle, annular, dark-field scanning TEM (HAADF-STEM) measurements (Fig. 1d–f) with sub-angstrom resolutions. Two regions clearly appear in these images; broad, curved, dark lines and small bright spots sized less than ~0.5 nm. The dark regions correspond to the projections of the nanotube walls along the incident electron beam direction, whereas the bright spots indicate that isolated heavier atoms were present, which were Re atoms in this case. Since the bright spots are not concentrated on the outer/inner surfaces of the nanotube walls but are rather uniform throughout the walls, one can conclude that the Re atoms were uniformly distributed along the nanotube walls with single-site states. The inductively coupled plasma (ICP) measurements show that the Re loadings were 0.288, 0.286, 0.294, and 0.291 mmol g<sup>-1</sup> for Re-BPy<sub>0.1</sub>-SNT, Re-BPy<sub>0.1</sub>-NT, Re-BPy<sub>0.3</sub>-NT, and Re-BPy<sub>0.3</sub>-NT-Me, respectively (Table S1). According to the CHN elemental analysis, the bpy<sub>Without coordination</sub>/bpy<sub>Total</sub> molar ratios for each catalyst were determined to be 42%, 38%, 73%, and 75%, respectively.

To further demonstrate the geometric structure of molecular Re on the skeleton of organosilica nanotubes, various spectroscopies were performed on Re-BPy<sub>0.3</sub>-NT-Me and Re(bpy)(CO)<sub>3</sub>Cl. In contrast with that of BPy<sub>0.3</sub>-NT, the Fourier transform infrared (FT-IR) spectrum (Fig. 2a) of Re-BPy<sub>0.3</sub>-NT-Me exhibits two new absorption peaks at approximately 1921 and 2028 cm<sup>-1</sup>, which were assigned to the vibration of the Re-CO ligands, in accordance with that of homogeneous Re(bpy)(CO)<sub>3</sub>Cl. The UV-vis diffuse reflectance spectrum (Fig. 2b) of

Re-BPy<sub>0.3</sub>-NT-Me shows a new absorption band appeared at approximately 400 nm compared with that of BPy<sub>0.3</sub>-NT, similar to that of homogeneous Re(bpy)(CO)<sub>3</sub>Cl, which could be assigned to the metal-to-ligand (*i.e.*, Re-to-bipyridine-ligand) charge transfer (MLCT) [14,24,26].

The X-ray absorption near-edge structure spectroscopies (XANES) show that the white line resonance peak at approximately 10,538 eV, which is assigned to the allowed 2p–5d transition, intensified with the increase in the d-band vacancies resulting from oxidation (Fig. 2c). Thus, the white line absorption peaks of oxidized Re species are more intense than those of the reduced species, which agrees well with the XPS results. Furthermore, more detailed structural information was obtained via extended X-ray absorption fine structure spectroscopy (EXAFS). In the Fourier transform of the Re L<sub>III</sub>-edge extended EXAFS spectra of Re(bpy)(CO)<sub>3</sub>Cl and Re-BPy<sub>0.3</sub>-NT-Me (Fig. 2d), three strong peaks appear at approximately 0.165, 0.220, and 0.264 nm, which can be assigned to Re-C, Re-N, and Re-Cl bond lengths, respectively [14,26]. The XANES spectra and EXAFS Fourier transform at the Re L<sub>III</sub>-edge show spectral features corresponding to those of the complex Re(bpy)(CO)<sub>3</sub>Cl, suggesting the successful formation of the desired Re complex on the pore surface of BPy-NT.

To prove the hydrophobicity/hydrophilicity of the as-prepared catalysts, water contact angles were measured (Fig. 3a). Organosilica nanotubes with benzene groups in the skeleton exhibit a significantly higher contact angle and thus higher hydrophobicity than pure silicon nanotubes. More importantly, Re-BPy<sub>0.3</sub>-NT-Me end-capped using trimethylsilyl [-Si(CH<sub>3</sub>)<sub>3</sub>] groups shows the strongest hydrophobicity, with a water contact angle of 96°. These results indicate that hydrophilicity/hydrophobicity can be regulated by finely tuning the matrix framework compositions.

In addition, gas sorption using water and benzene was measured at 298 K. As shown in Fig. 3b, c, Re-BPy<sub>0.1</sub>-NT and Re-BPy<sub>0.3</sub>-NT exhibit lower water adsorption and higher benzene adsorption at P/P<sub>0</sub> = 0.97 than Re-BPy<sub>0.1</sub>-SNT. Clearly, Re-BPy<sub>0.3</sub>-NT-Me shows the lowest water adsorption (35.3 cm<sup>3</sup>/g) and highest benzene adsorption (138.9 cm<sup>3</sup>/g) at P/P<sub>0</sub> = 0.97 because of the improved hydrophobicity. In addition, the CO<sub>2</sub> uptake performances of all the materials were investigated at 298 K (Fig. 3d). The adsorption capacities of Re-BPy<sub>0.3</sub>-NT-Me and Re-BPy<sub>0.3</sub>-NT were 13.2 and 10.7 mL/g, respectively, which were significantly higher than those of Re-BPy<sub>0.1</sub>-NT and Re-BPy<sub>0.1</sub>-SNT. The higher CO<sub>2</sub> adsorption capacities of

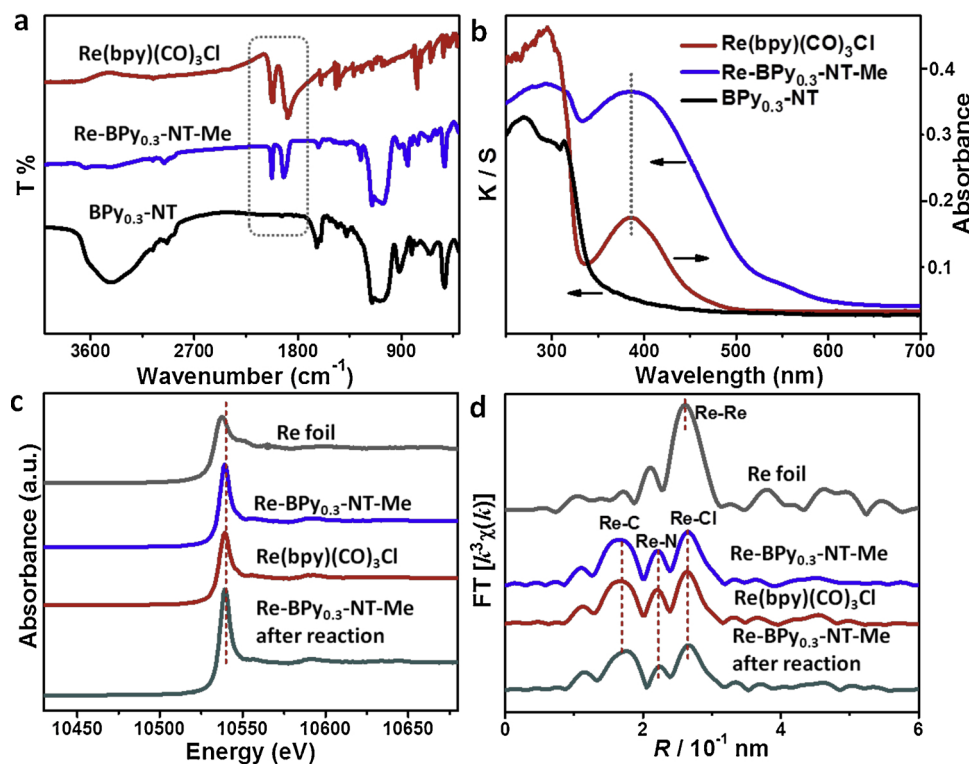


**Fig. 2.** (a) FT-IR and (b) UV-vis diffuse reflectance spectra of BPY<sub>0.3</sub>-NT, Re-BPY<sub>0.3</sub>-NT-Me, and Re(bpy)(CO)<sub>3</sub>Cl. (c) Re L<sub>III</sub>-edge XANES spectra, and (d) Fourier transform EXAFS spectra of Re(bpy)(CO)<sub>3</sub>Cl, Re-BPY<sub>0.3</sub>-NT-Me and Re-BPY<sub>0.3</sub>-NT-Me after reaction.

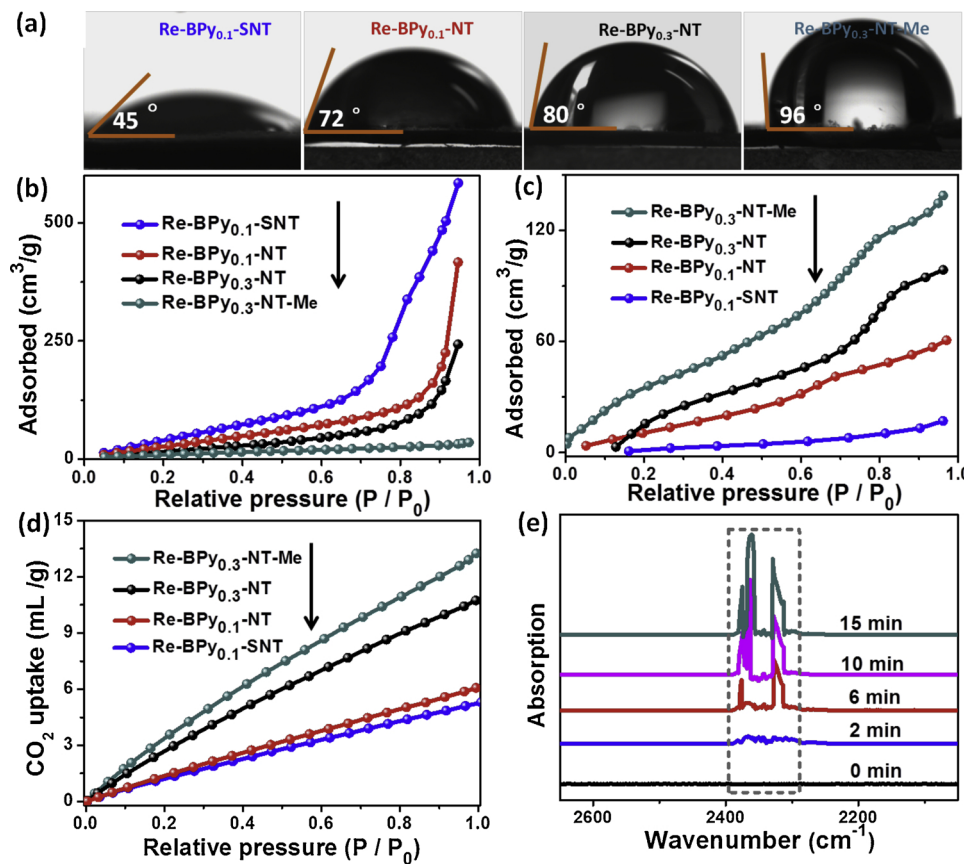


**Fig. 3.** (a) Contact angle measurements of Re-BPy<sub>0.1</sub>-SNT, Re-BPy<sub>0.1</sub>-NT, Re-BPy<sub>0.3</sub>-NT and Re-BPy<sub>0.3</sub>-NT-Me at 298 K. (b) Water and (c) benzene sorption measurements and (d) CO<sub>2</sub> uptake performance of Re-BPy<sub>0.1</sub>-SNT, Re-BPy<sub>0.1</sub>-NT, Re-BPy<sub>0.3</sub>-NT, and Re-BPy<sub>0.3</sub>-NT-Me at 298 K. (e) *In situ* infrared of CO<sub>2</sub> for pure 2,2'-bipyridine at 298 K.

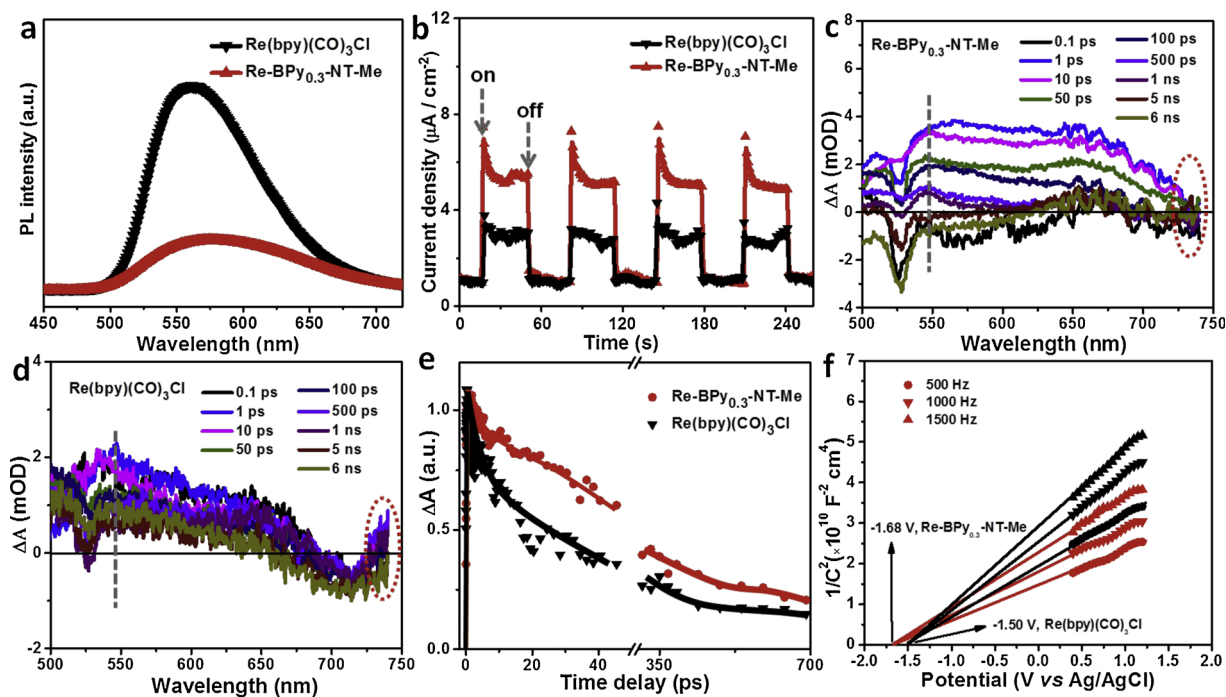


**Fig. 4.** (a) PL spectra, (b) Transient photocurrent responses, (c), (d) Transient optical spectra in the presence of a sacrificial electron donor TEOA, (e) Comparison of kinetics for intramolecular charge transfer at 550 nm and (f) Mott-Schottky plots of Re(bpy)(CO)<sub>3</sub>Cl and Re-BPy<sub>0.3</sub>-NT-Me.

Re-BPy<sub>0.3</sub>-NT-Me and Re-BPy<sub>0.3</sub>-NT could be primarily attributed to the more bipyridine ligands in their frameworks, which can effectively improve the CO<sub>2</sub> uptake (Fig. 3e, Table S1).

The optical properties of Re-BPy<sub>0.3</sub>-NT-Me were investigated by photoluminescence (PL) spectroscopy, as shown in Fig. 4a. Re-BPy<sub>0.3</sub>-NT-Me exhibits a lower PL intensity than homogeneous Re(bpy)(CO)<sub>3</sub>Cl when irradiated by a 380-nm laser, with a peak centered at 575 nm, which can be attributed to the efficient photoinduced charge transfer process resulting from the inhibition of intermolecular aggregation by the heterogenization of the catalyst. The transient photocurrent response was also performed to study the photogenerated charge transfer and separation efficiency (Fig. 4b). The photocurrent immediately increased when the light irradiation was turned on, while the photocurrent quickly decreased when the light was switched off, which demonstrates the existence of the photoresponse for Re-BPy<sub>0.3</sub>-NT-Me. The heterogeneous molecular Re-BPy<sub>0.3</sub>-NT-Me shows a photocurrent density of approximately 5.5 μA/cm<sup>2</sup>, which is higher than the complex Re(bpy)(CO)<sub>3</sub>Cl (3.0 μA/cm<sup>2</sup>), indicating the efficient photogenerated charge transfer and separation in Re-BPy<sub>0.3</sub>-NT-Me.

To further study light absorption and intramolecular charge transfer (ICT) of Re-BPy<sub>0.3</sub>-NT-Me, the transient absorption (TA) spectroscopies were performed with a 380 nm excitation (Fig. 4c, d). A stronger and broader positive transient signal in the 550–700 nm region assigned to the absorption of excited ICT appears for Re-BPy<sub>0.3</sub>-NT-Me compared with the complex Re(bpy)(CO)<sub>3</sub>Cl [20], which may be mainly due to the fact that the heterogeneous molecular complex has longer lifetime in the excited ICT states than Re(bpy)(CO)<sub>3</sub>Cl. The TA of Re(bpy)(CO)<sub>3</sub>Cl shows a positive transient signal in the > 725 nm region, which can be assigned to the formation of catalytically inactive Re-dimers [28], whereas Re-BPy<sub>0.3</sub>-NT-Me did not have this transient signal due to isolated active sites. Furthermore, the corresponding kinetics comparison of ICT for Re-BPy<sub>0.3</sub>-NT-Me and Re(bpy)(CO)<sub>3</sub>Cl were also performed. As shown in Fig. 4e, the formation (rising component) of the excited ICT is ultrafast with ~300 fs for both samples. But interestingly, this excited ICT state of Re-BPy<sub>0.3</sub>-NT-Me exhibits much longer lifetime ( $t = 161.5$  ps) than that of the complex Re(bpy)(CO)<sub>3</sub>Cl ( $t = 24.8$  ps), suggesting that the heterogenization of Re(bpy)(CO)<sub>3</sub>Cl

could effectively inhibit charge recombination in Re-BPy<sub>0.3</sub>-NT-Me. In addition, Mott-Schottky measurements were applied to investigate the electronic band positions and corresponding redox abilities of Re-BPy<sub>0.3</sub>-NT-Me and Re(bpy)(CO)<sub>3</sub>Cl (Fig. 4f). The flat band positions are  $-1.68$  and  $-1.50$  V (vs Ag/AgCl) for Re-BPy<sub>0.3</sub>-NT-Me and Re(bpy)(CO)<sub>3</sub>Cl, respectively, according to extrapolation of  $C^{2-}$  values at frequencies of 500, 1000, and 1500 Hz. The positive slopes reveal n-type-like conductivities of Re-BPy<sub>0.3</sub>-NT-Me and Re(bpy)(CO)<sub>3</sub>Cl. For n-type semiconductors, the flat band potential is generally approximated by the conduction band potential. Obviously, both samples show more negative reduction potentials ( $-1.48$  V vs NHE for Re-BPy<sub>0.3</sub>-NT-Me and  $-1.30$  V vs NHE for Re(bpy)(CO)<sub>3</sub>Cl) than CO<sub>2</sub>/CO ( $-0.53$  V vs NHE), suggesting the feasibility for photoreduction of CO<sub>2</sub> to CO.

Subsequently, the performances (Fig. S18) of these Re-based catalysts for the photochemical reduction of CO<sub>2</sub> were investigated at room temperature with visible light ( $\lambda > 420$  nm) illumination in a CO<sub>2</sub>-saturated acetonitrile-water solution ( $V_{\text{MeCN}}/V_{\text{H}_2\text{O}} = 0.875/1$ ). Fig. 5a shows the CO-TON, H<sub>2</sub>-TON and CO selectivity with different catalysts under similar reaction conditions at 8 h. No other liquid phase products were detected (Fig. S19). The CO-TON (15.20) of Re-BPy<sub>0.3</sub>-NT was higher than that of Re-BPy<sub>0.1</sub>-NT (10.72). The higher catalytic activity of Re-BPy<sub>0.3</sub>-NT could be attributed to a higher number of bipyridine ligands in the framework (increase CO<sub>2</sub> adsorption) and the shorter nanotube length (decrease the diffusion path of reactants and products during the reactions). Notably, the Re-BPy<sub>0.3</sub>-NT-Me with the capped silanol exhibited the highest CO-TON (19.30) and lowest H<sub>2</sub>-TON (1.23) with the CO producing rate of 700 μmol/g/h. A CO selectivity as high as 94% could be achieved even in the high water-containing system (50% volume ratio, Table 1). This high selectivity can be explained by the precise modulation of the surface physiochemical properties. When the silanol was capped by methyl groups, the high hydrophobicity of Re-BPy<sub>0.3</sub>-NT-Me could effectively prevent H<sub>2</sub>O molecules from reaching the catalytic active centers for H<sup>+</sup> reduction. In contrast, CO<sub>2</sub> molecules can easily approach the Re sites, thus facilitating the CO<sub>2</sub> reduction owing to the enhanced role of CO<sub>2</sub> in the competition for adsorption sites. To further prove the hydrophobic/hydrophilic effect, the catalyst with pure silica

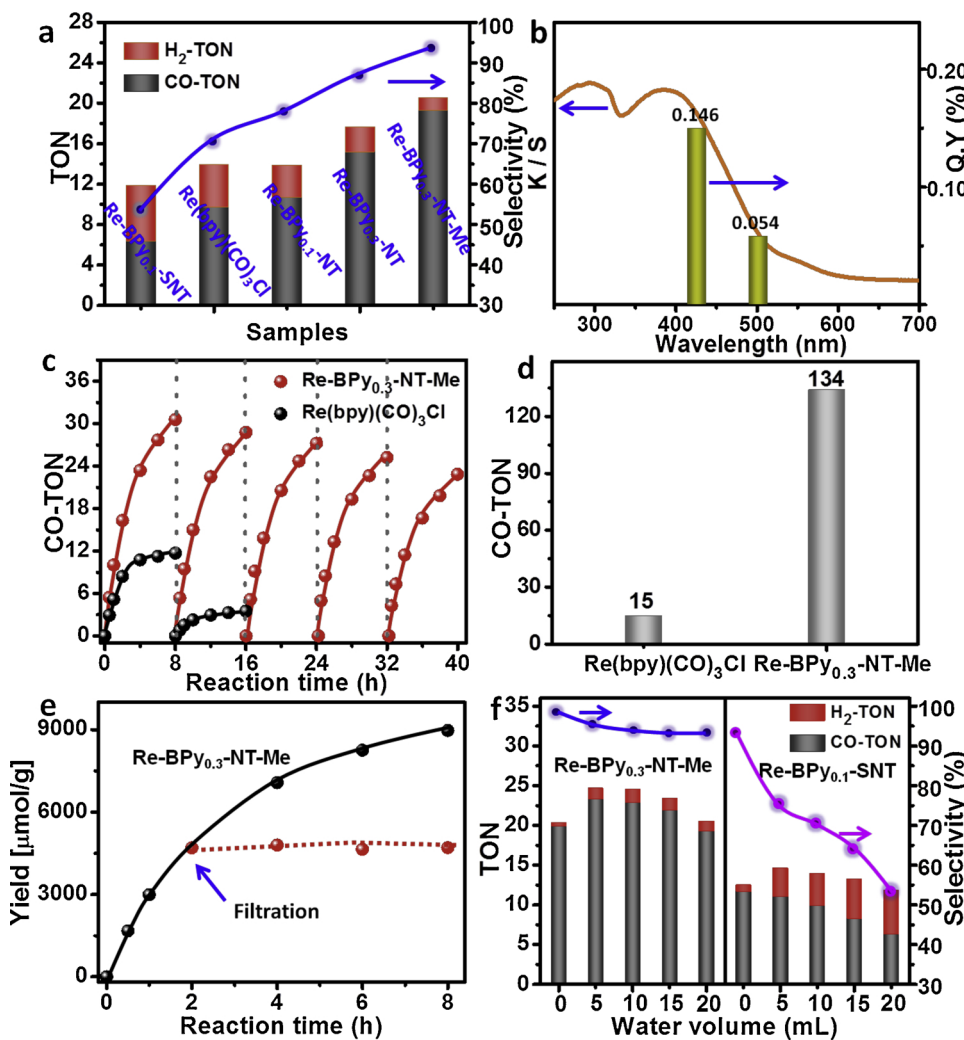


**Fig. 5.** (a) The CO-TON, H<sub>2</sub>-TON and CO selectivity of Re-BPy<sub>0.1</sub>-SNT, Re(bpy)(CO)<sub>3</sub>Cl, Re-BPy<sub>0.1</sub>-NT, Re-BPy<sub>0.3</sub>-NT and Re-BPy<sub>0.3</sub>-NT-Me after 8 h at 298 K with 20 mL of water and 2.9 μmol Re. (b) Dependence of the QYs of the Re-BPy<sub>0.3</sub>-NT-Me on the wavelength of monochromatic light irradiation (435, 500 nm)  $QY = 2n_{co}/n_{incident photons} \times 100\%$ . (c) Recycling performance, (d) The total CO-TON and (e) filtration experiment of Re-BPy<sub>0.3</sub>-NT-Me for the photochemical reduction of CO<sub>2</sub> with 1.0 μmol Re. (f) Effect of water on the CO-TON, H<sub>2</sub>-TON and CO selectivity for the Re-BPy<sub>0.3</sub>-NT-Me and Re-BPy<sub>0.1</sub>-SNT at 298 K with 2.9 μmol Re for the photochemical reduction CO<sub>2</sub> (the total volume of solution is 40 mL).

**Table 1**  
Comparison of catalyst properties during the photochemical reduction CO<sub>2</sub>.<sup>a</sup>

Entry	Photocatalyst	H <sub>2</sub> -TON <sup>b</sup>	CO-TON <sup>c</sup>	Selectivity (%)
1	Re-BPy <sub>0.3</sub> -NT-Me	1.23	19.30	94
2	Re-BPy <sub>0.3</sub> -NT	2.44	15.20	86
3	Re-BPy <sub>0.1</sub> -NT	3.16	10.72	77
4	Re-BPy <sub>0.1</sub> -SNT	5.56	6.32	53
5	Re(bpy)(CO) <sub>3</sub> Cl	4.18	9.64	70
6	–	0	0	–
7	BPy <sub>0.3</sub> -NT	0	0	–
8	Re-BPy <sub>0.3</sub> -NT-Me/ no CO <sub>2</sub>	1.41	0	0
9	Re-BPy <sub>0.3</sub> -NT-Me/ no light	0	0	–
10	Re-BPy <sub>0.3</sub> -NT-Me/ no TEOA	0	0	–
11	Re-BPy <sub>0.3</sub> -NT-Me/2.0 μmol Re	1.48	24.21	94
12	Re-BPy <sub>0.3</sub> -NT-Me/1.0 μmol Re	1.94	30.60	94

<sup>a</sup> Reaction conditions: 2.9 μmol of Re, 2.5 mL of TEOA, 17.5 mL of CH<sub>3</sub>CN, 20 mL of H<sub>2</sub>O, and λ > 420 nm, at room temperature.

<sup>b</sup> H<sub>2</sub>-TON is defined as the number of evolved hydrogen molecules per catalytic site (Re).

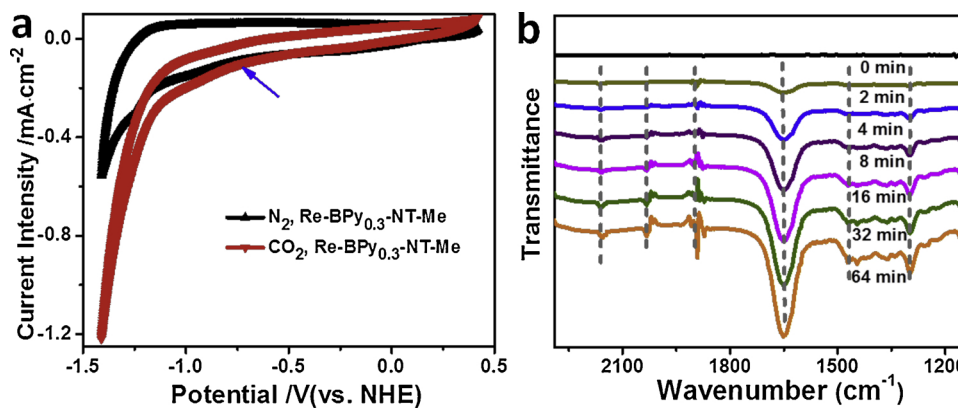
<sup>c</sup> CO-TON is defined as the number of evolved CO molecules per catalytic site (Re).

nanotubes but no phenyl groups (Re-BPy<sub>0.1</sub>-SNT) was used to photocatalyze the CO<sub>2</sub>-CO reaction under the same reaction conditions. It can be seen that Re-BPy<sub>0.1</sub>-SNT exhibited the lowest CO-TON (6.32) and highest H<sub>2</sub>-TON (5.56), with a CO selectivity of 53% (Fig. 5a), which could be mainly attributed to the high hydrophilicity of the pure silica nanotube framework. For comparison, the homogeneous catalyst

Re(bpy)(CO)<sub>3</sub>Cl was also used to photocatalyze the same reaction. Unfortunately, Re(bpy)(CO)<sub>3</sub>Cl became inactive after 4 h of reaction (Fig. S18) and showed a lower CO selectivity of 70%, owing to the decomposition via bimolecular pathways to form metal nanoparticles (Figs. S20, S28) [22,25,27,29,32]. These above results demonstrated the excellent catalytic performance of Re-BPy<sub>0.3</sub>-NT-Me for the CO<sub>2</sub>-CO reaction owing to the heterogenization of the molecular catalyst and the finely tuned microenvironment around the active species. In addition, the quantum yields (QYs) strongly depend on the intensity of irradiated light (Fig. 5b). In particular, the QYs of Re-BPy<sub>0.3</sub>-NT-Me can be as high as 0.146% under 435-nm monochromatic light irradiation.

After the reaction, Re-BPy<sub>0.3</sub>-NT-Me was reused for the next run, and the solid catalyst retained high catalytic activity (Fig. 5c). During the fifth recycle, CO-TON was maintained at approximately 22.85, showing a slight decrease. The total TON reached 134 within 40 h (Fig. 5d). In contrast, the homogeneous catalyst showed a large decrease in CO-TON for the first recycle and was fully deactivated after the second reuse (15 of the total TON, Fig. 5d). In addition, the filtration experiment indicated that the catalytic activity came from Re-BPy<sub>0.3</sub>-NT-Me, and the solid catalyst was truly heterogeneous (Fig. 5e). The structure analysis of Re-BPy<sub>0.3</sub>-NT-Me after the reaction revealed the molecular nature of the active site without the formation of Re nanoparticles, as well as the stable nanotube frameworks (Fig. 2c, d, Figs. S20–27).

To demonstrate the effect of hydrophobicity/hydrophilicity on the reaction pathways, the effect of the amount of water on the CO-TON,



H<sub>2</sub>-TON and CO selectivity in this reaction system was investigated using Re-BPy<sub>0.3</sub>-NT-Me and Re-BPy<sub>0.1</sub>-SNT as control catalysts (Fig. 5f). Surprisingly, adding water can improve the catalytic performance of the hydrophobic Re-BPy<sub>0.3</sub>-NT-Me catalyst to some extent, mainly due to that the added water could promote the proton-coupled electron transfer [35–40]. Furthermore, the presence of the proton-coupled electron transfer effect was also confirmed by the photocurrent response test (Fig. S29). A high CO selectivity over 94% can be obtained with a high CO-TON over 18 and an almost constant H<sub>2</sub>-TON below 1.5 in 0–20 mL of water. However, for the hydrophilic Re-BPy<sub>0.1</sub>-SNT, the CO selectivity and CO-TON always decrease, whereas H<sub>2</sub>-TON increases with the addition of water. These results indicate that the hydrophobic Re-BPy<sub>0.3</sub>-NT-Me catalyst can achieve high activity and selectivity in a system with a high concentration of water by fine-tuning the microenvironment around the active species, which provides a promising platform to design devices for artificial photosynthesis.

Next, the redox properties of Re-BPy<sub>0.3</sub>-NT and Re-BPy<sub>0.3</sub>-NT-Me were investigated by recording cyclic voltammograms (CVs) to further illustrate the effect of hydrophobicity on CO<sub>2</sub> reduction (Fig. 6a and Fig. S30). The CV of Re-BPy<sub>0.3</sub>-NT-Me exhibits increased current at E<sub>onset</sub> = −0.74 V under a CO<sub>2</sub> atmosphere, and this current density (−1.22 mA/cm<sup>2</sup>) is more than 2.3 times higher than that under an N<sub>2</sub> atmosphere. Interestingly, Re-BPy<sub>0.3</sub>-NT-Me exhibits a lower E<sub>onset</sub> and higher current density than Re-BPy<sub>0.3</sub>-NT (−0.80 V and −0.94 mA/cm<sup>2</sup>, respectively) and Re(bpy)(CO)<sub>3</sub>Cl (−0.82 V and −0.82 mA/cm<sup>2</sup>, respectively). These results indicate that hydrophobic Re-BPy<sub>0.3</sub>-NT-Me is more favorable for CO<sub>2</sub> reduction.

To further investigate the photocatalytic CO<sub>2</sub> reduction process, *in situ* infrared spectroscopy was conducted for the Re-BPy<sub>0.3</sub>-NT-Me sample (Fig. 6b). Some new peaks clearly emerge with the increased irradiation time from 0 to 64 min; the peaks at 1297, 1473, and 1650 cm<sup>-1</sup> are assigned to the Re-COOH groups [41–44]. The intensity of these peaks increased with increasing exposure time, suggesting that the Re-COOH groups are intermediates during the photoreduction of CO<sub>2</sub> to CO. Subsequently, the Re-COOH species accepts another proton and undergoes dehydration to form a Re-CO complex, which gives rise to some additional peaks at 1870–2050 cm<sup>-1</sup>. Finally, the CO molecule in Re-CO can be readily released and desorbed from the catalyst surface, as indicated by the peak at 2160 cm<sup>-1</sup> [41–44].

Based on the experimental results, a possible mechanism underlying the photocatalytic reduction of CO<sub>2</sub> in a system containing such a high concentration of water is proposed in Fig. 7a. First, the initial Re complex A is converted into the one-electron reduced species B after irradiation with visible light based on the MLCT. Then, species B is reductively quenched using TEOA to form species C. Subsequently, the CO<sub>2</sub> adduct D is formed by the nucleophilic attack of the Re complex C on the electrophilic carbon atom of CO<sub>2</sub>, accompanied by coordination with H<sup>+</sup> of H<sub>2</sub>O. The CO<sub>2</sub> adduct D can accept another H<sup>+</sup> from H<sub>2</sub>O to form intermediate species E, thus driving the CO<sub>2</sub> reduction. Finally,

the ligand exchange of the molecular CO of species E with Cl<sup>−</sup> produces the initial Re complex A to complete the CO<sub>2</sub> reduction pathway (1). Evidently, adding water plays a proton-promoting role. Simultaneously, protons are reduced to form H<sub>2</sub> (pathway (2)) during this process, which is the main reaction competing with the CO<sub>2</sub> reduction [17–19,45]. Interestingly, for hydrophobic Re-BPy<sub>0.3</sub>-NT-Me, more CO<sub>2</sub> and fewer protons are allowed to reach the active site to react; thus, water primarily play a proton-promoting role. However, for hydrophilic Re-BPy<sub>0.1</sub>-SNT, excess protons can reach the active sites, resulting in more competition between the two reactions (1 and 2), thus weakening the reduction of CO<sub>2</sub> (1).

In addition, density functional theory (DFT) calculations were employed to investigate the binding energies of H<sub>2</sub>O onto the Re-BPy<sub>0.3</sub>-NT and Re-BPy<sub>0.3</sub>-NT-Me. As shown in Fig. 7b, the binding energy of H<sub>2</sub>O on Re-BPy<sub>0.3</sub>-NT is −0.48 eV, which is much stronger than that of Re-BPy<sub>0.3</sub>-NT-Me (−0.28 eV). Further, such an obvious difference in the binding energy of H<sub>2</sub>O over Re-BPy<sub>0.3</sub>-NT and Re-BPy<sub>0.3</sub>-NT-Me has been proved by experimentally (Fig. 3a, b, and c). Notably, the weaker binding energy of H<sub>2</sub>O on Re-BPy<sub>0.3</sub>-NT-Me can suppress the undesired metal-H<sub>2</sub>O adduct F with H<sub>2</sub> as a by-product.

Finally, the evolution of the free energy of CO<sub>2</sub> photoreduction to CO on the Re-BPy<sub>0.3</sub>-NT-Me was calculated using DFT to better evaluate and understand the reaction processes and related active species (Fig. 7c). As shown in Fig. 7c, the pathway for the reduction of CO<sub>2</sub> to CO via a Re-carboxyl (Re-COOH\*) intermediate via the transfer of two protons and electrons was considered. Initially, the CO<sub>2</sub> molecule is adsorbed on the Re sites, with concerted protonation and electron transfer, leading to the formation of the Re-COOH\* intermediate. Subsequently, this intermediate can be further reduced via proton–electron transfer to form a Re-CO\* adduct, releasing one H<sub>2</sub>O molecule. Here, it should be mentioned that the hydrophobic material Re-BPy<sub>0.3</sub>-NT-Me facilitates the separation of water from the reaction system, thereby accelerating the reaction. The main product CO is finally generated from the ligand exchange of the molecular CO of species E with Cl<sup>−</sup>. We find that the formation of the Re-COOH\* species via protonation (energy barrier of 0.39 eV) and the release of molecular CO via the ligand exchange (energy barrier of 0.46 eV) are the two main rate-limiting steps. Importantly, adding weak Bronsted acids (H<sub>2</sub>O) can effectively facilitate these catalytic pathways. On the one hand, adding water provides more protons to accelerate the formation of the Re-COOH\* intermediate via the protonation of CO<sub>2</sub>. On the other hand, the protons H<sup>+</sup> from the H<sub>2</sub>O can further promote the conversion of ReOH\* to Re-CO\*. As a result, the concentration of Re-CO\* will continue to increase, thereby accelerating the release of CO according to reaction equilibrium theory. However, the DFT calculations of the free energy evolution of protons reducing to H<sub>2</sub> indicate that reducing protons is easier than reducing CO<sub>2</sub> in this system (Fig. S31), which is the main competitive reaction for CO<sub>2</sub> reduction. In response to this problem, adjusting the microenvironment around the active sites will provide

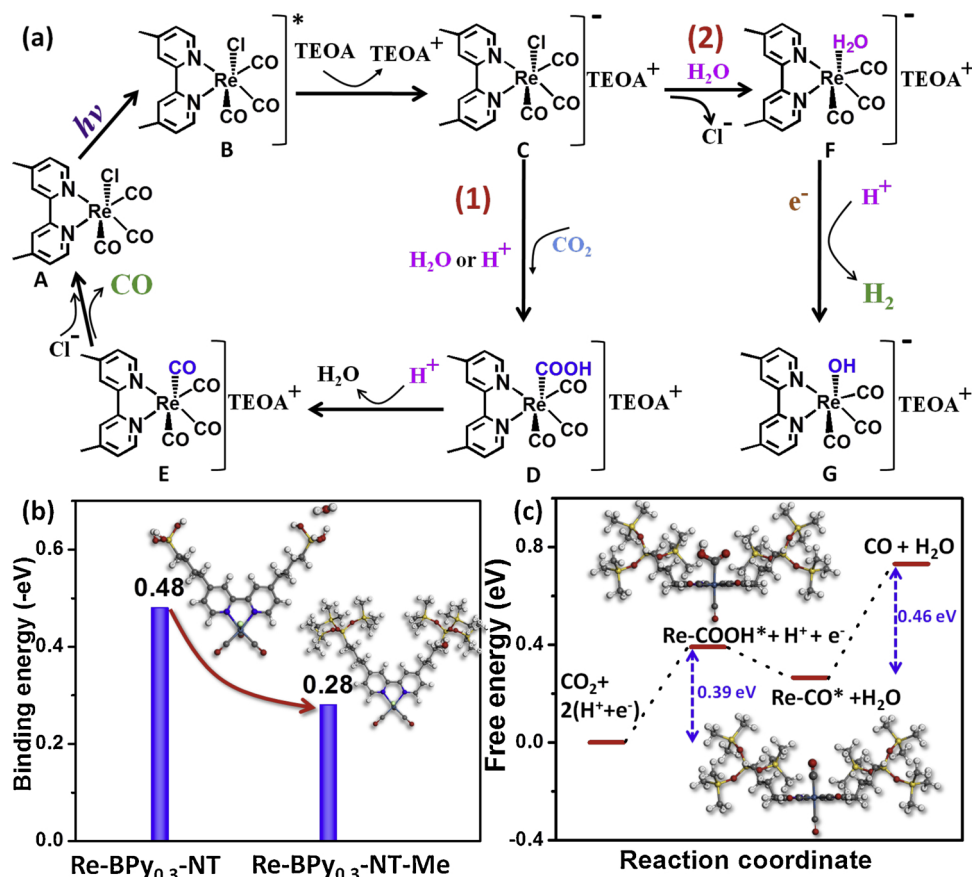


**Fig. 7.** (a) Possible photocatalytic CO<sub>2</sub> reduction mechanism. DFT calculations: (b) the binding energy of H<sub>2</sub>O onto Re-BPy<sub>0.3</sub>-NT and Re-BPy<sub>0.3</sub>-NT-Me and (c) free energy evolution of the reduction of CO<sub>2</sub> to CO on Re-BPy<sub>0.3</sub>-NT-Me.

obvious advantages. Furthermore, it must be mentioned that the desorption of CO intermediates on the molecular catalyst is also very important for photoreduction CO<sub>2</sub> to CO [13,18,20]. Through the hydrophobicity regulation, we hope to reduce the competitive reaction of water, and also hope not to reduce the desorption process of the product CO. Fortunately, the DFT results show that binding energy of Re-CO on the Re-BPy<sub>0.3</sub>-NT-Me and Re-BPy<sub>0.3</sub>-NT is -1.15 eV and -1.08 eV (Fig. S32), respectively, which indicates that the desorption of product CO on the molecular catalyst is relatively similar. Therefore, we believe that the improvement of CO<sub>2</sub> reduction performance for the modified Re-BPy<sub>0.3</sub>-NT-Me material is mainly by reducing the competitive reaction of H<sub>2</sub>O according to the DFT and experimental results. For the optimized Re-BPy<sub>0.3</sub>-NT-Me, such a microenvironment can not only prevent excessive protons from reacting on the active site owing to high hydrophobicity but also effectively increase the adsorption capacity of CO<sub>2</sub> owing to more bipyridine on the skeleton, thus playing a dual role.

#### 4. Conclusion

In conclusion, we have constructed efficient heterogeneous molecular rhodium catalysts based on organosilica nanotubes and proposed a microenvironment modification strategy to tune the surface compositions for the highly selective photoreduction of CO<sub>2</sub> in aqueous solutions. By adjusting the bipyridine contents in the framework of organosilica nanotubes and subsequently capping the surface silanols, we modulated the CO<sub>2</sub> adsorption capacity and hydrophobicity/hydrophilicity around the active sites, leading to a high CO selectivity of 94% in a photocatalytic CO<sub>2</sub> reduction system with a high concentration of water. DFT calculations and *in situ* infrared spectroscopy reveal that the binding energy of H<sub>2</sub>O decreased considerably, and the main

intermediate was Re-COOH\* via the protonation of CO<sub>2</sub> after modifying the microenvironment around the active sites. We believe that this work will provide a new guideline for the device design using functional organosilica nanotubes as highly tunable one-dimensional catalytic materials for artificial photosynthesis.

#### Declaration of Competing Interest

The authors declare no competing financial interests.

#### Acknowledgments

We acknowledge the National Natural Science Foundation of China (U1662109) for financial support. The Program of Introducing Talents of Discipline to Universities of China (111 program, <GN2> B17019) </GN2> is also acknowledged.

#### Appendix B. Supplementary data

Supplementary material related to this article can be found, in the online version, at doi:<https://doi.org/10.1016/j.apcatb.2019.118113>.

#### References

- [1] X. Liu, S. Inagaki, J. Gong, Angew. Chem. Int. Ed. 55 (2016) 14924–14950.
- [2] N. Elgrishi, M.B. Chambers, X. Wang, M. Fontecave, Chem. Soc. Rev. 46 (2017) 761–796.
- [3] S. Berardi, S. Drouet, L. Francas, C. Gimbert-Surinach, M. Guttentag, C. Richmond, T. Stoll, A. Llobet, Chem. Soc. Rev. 43 (2014) 7501–7519.
- [4] X. Chang, T. Wang, J. Gong, Energy Environ. Sci. 9 (2016) 2177–2196.
- [5] X. Liu, F. Kang, C. Hu, L. Wang, Z. Xu, D. Zheng, W. Gong, Y. Lu, Y. Ma, J. Wang, Nat. Chem. 10 (2018) 1201–1206.
- [6] M. Aresta, A. Dibenedetto, A. Angelini, Chem. Rev. 114 (2014) 1709–1742.

[7] E.E. Benson, C.P. Kubiak, A.J. Sathrum, J.M. Smieja, *Chem. Soc. Rev.* 38 (2009) 89–99.

[8] K.A. Grice, *Coord. Chem. Rev.* 336 (2017) 78–95.

[9] A.J. Morris, G.J. Meyer, E. Fujita, *Acc. Chem. Res.* 42 (2009) 1983–1994.

[10] M.L. Clark, A. Ge, P.E. Videla, B. Rudshteyn, C.J. Miller, J. Song, V.S. Batista, T. Lian, C.P. Kubiak, *J. Am. Chem. Soc.* 140 (2018) 17643–17655.

[11] B. Reuillard, K.H. Ly, T.E. Rosser, M.F. Kuehnle, I. Zebger, E. Reisner, *J. Am. Chem. Soc.* 139 (2017) 14425–14435.

[12] K.M. Choi, D. Kim, B. Rungtaweevoranit, C.A. Trickett, J.T. Barmanbek, A.S. Alshammari, P. Yang, O.M. Yaghi, *J. Am. Chem. Soc.* 139 (2017) 356–362.

[13] B. Zhang, L. Sun, *Chem. Soc. Rev.* 48 (2019) 2216–2264.

[14] M. Waki, K.I. Yamanaka, S. Shirai, Y. Maegawa, Y. Goto, Y. Yamada, S. Inagaki, *Chem. Eur. J.* 24 (2018) 3846–3853.

[15] R. Kuriki, M. Yamamoto, K. Higuchi, Y. Yamamoto, M. Akatsuka, D. Lu, S. Yagi, T. Yoshida, O. Ishitani, K. Maeda, *Angew. Chem. Int. Ed.* 56 (2017) 4867–4871.

[16] S. Fukuzumi, Y.M. Lee, H.S. Ahn, W. Nam, *Chem. Sci.* 9 (2018) 6017–6034.

[17] S. Sato, T. Morikawa, T. Kajino, O. Ishitani, *Angew. Chem. Int. Ed.* 52 (2013) 988–992.

[18] T. Ouyang, H.-H. Huang, J.-W. Wang, D.-C. Zhong, T.-B. Lu, *Angew. Chem. Int. Ed.* 56 (2017) 738–743.

[19] M. Liu, Y.-F. Mu, S. Yao, S. Guo, X.-W. Guo, Z.-M. Zhang, T.-B. Lu, *Appl. Catal. B* 245 (2019) 496–501.

[20] S. Yang, W. Hu, X. Zhang, P. He, B. Pattengale, C. Liu, M. Cendejas, I. Hermans, X. Zhang, J. Zhang, J. Huang, *J. Am. Chem. Soc.* 140 (2018) 14614–14618.

[21] Y. Wang, N.Y. Huang, J.Q. Shen, P.Q. Liao, X.M. Chen, J.P. Zhang, *J. Am. Chem. Soc.* 140 (2018) 38–41.

[22] X. Liu, Y. Maegawa, Y. Goto, K. Hara, S. Inagaki, *Angew. Chem. Int. Ed.* 55 (2016) 7943–7947.

[23] G. Jiang, K. Geng, Y. Wu, Y. Han, X. Shen, *Appl. Catal. B* 227 (2018) 366–375.

[24] H.-P. Liang, A. Acharya, D.A. Anito, S. Vogl, T.-X. Wang, A. Thomas, B.-H. Han, *ACS Catal.* 9 (2019) 3959–3968.

[25] Y. Ueda, H. Takeda, T. Yui, K. Koike, Y. Goto, S. Inagaki, O. Ishitani, *ChemSusChem* 8 (2015) 439–442.

[26] M. Wen, K. Mori, Y. Kuwahara, H. Yamashita, *ChemCatChem* 7 (2015) 3519–3525.

[27] C. Wang, Z. Xie, K.E. deKrafft, W. Lin, *J. Am. Chem. Soc.* 133 (2011) 13445–13454.

[28] C.D. Windle, E. Pastor, A. Reynal, A.C. Whitwood, Y. Vaynzof, J.R. Durrant, R.N. Perutz, E. Reisner, *Chem. Eur. J.* 21 (2015) 3746–3754.

[29] S. Zhang, H. Wang, M. Li, J. Han, X. Liu, J. Gong, *Chem. Sci.* 8 (2017) 4489–4496.

[30] S. Zhang, H. Wang, L. Tang, M. Li, J. Tian, Y. Cui, J. Han, X. Zhu, X. Liu, *Appl. Catal. B* 220 (2018) 303–313.

[31] S. Zhang, X. Liu, M. Li, Y. Wei, G. Zhang, J. Han, X. Zhu, Q. Ge, H. Wang, *Catal. Today* 324 (2019) 59–65.

[32] S. Zhang, H. Wang, M. Li, J. Han, S. Inagaki, X. Liu, *Dalton Trans.* 46 (2017) 9369–9374.

[33] S. Zhang, M. Li, Q. Wu, H. Yang, J. Han, H. Wang, X. Liu, *Appl. Catal. B* 236 (2018) 466–474.

[34] X. Liu, X.B. Li, Z. Guan, J. Liu, J. Zhao, Y. Yang, Q.H. Yang, *Chem. Commun.* 47 (2011) 8073–8075.

[35] O.S. Wenger, *Coord. Chem. Rev.* 282–283 (2015) 150–158.

[36] C.J. Gagliardi, B.C. Westlake, C.A. Kent, J.J. Paul, J.M. Papanikolas, T.J. Meyer, *Coord. Chem. Rev.* 254 (2010) 2459–2471.

[37] M.L. Clark, P.L. Cheung, M. Lessio, E.A. Carter, C.P. Kubiak, *ACS Catal.* 8 (2018) 2021–2029.

[38] J. Zhao, Q. Wang, C. Sun, T. Zheng, L. Yan, M. Li, K. Shao, X. Wang, Z. Su, *J. Mater. Chem. A* 5 (2017) 12498–12505.

[39] Y. Gao, L. Ye, S. Cao, H. Chen, Y. Yao, J. Jiang, L. Sun, *ACS Sustain. Chem. Eng.* 6 (2017) 781–786.

[40] C. Yang, Q. Li, Y. Xia, K. Lv, M. Li, *Appl. Surf. Sci.* 464 (2019) 388–395.

[41] J. Wang, T. Xia, L. Wang, X. Zheng, Z. Qi, C. Gao, J. Zhu, Z. Li, H. Xu, Y. Xiong, *Angew. Chem. Int. Ed.* 57 (2018) 16447–16689.

[42] W. Su, J. Zhang, Z. Feng, T. Chen, P. Ying, C. Li, *J. Phys. Chem. C* 112 (2008) 7710–7716.

[43] J. Wu, X. Li, W. Shi, P. Ling, Y. Sun, X. Jiao, S. Gao, L. Liang, J. Xu, W. Yan, C. Wang, Y. Xie, *Angew. Chem. Int. Ed.* 57 (2018) 8719–8723.

[44] G. Liu, X. Meng, H. Zhang, G. Zhao, H. Pang, T. Wang, P. Li, T. Kako, J. Ye, *Angew. Chem. Int. Ed.* 56 (2017) 5570–5574.

[45] P. Kurz, B. Probst, B. Spingler, R. Alberto, *Eur. J. Inorg. Chem.* 2006 (2006) 2966–2974.